Fully Integrated Time-Gated 3D Fluorescence Imager for Deep Neural Imaging

Jaebin Choi
Columbia University, NY, USA
jc3797@columbia.edu

Adriaan J. Taal
Columbia University, NY, USA
at3111@columbia.edu

Eric H. Pollmann
Columbia University, NY, USA
ehp2121@columbia.edu

William Meng
Columbia University, NY, USA
wlm2117@columbia.edu

Sajjad Moazeni
Columbia University, NY, USA
sm4659@columbia.edu

Laurent C. Moreaux
Cal. Ins. of Tech., Pasadena, USA
moreauxl@caltech.edu

Michael L. Roukes
Cal. Ins. of Tech., Pasadena, USA
roukes@caltech.edu

Kenneth L. Shepard
Columbia University, NY, US
shepard@ee.columbia.edu

Abstract—**This paper reports an implantable 3D imager for time-gated fluorescence imaging in the deep brain. Fluorescence excitation is provided by dual ns-pulsed blue micro-light-emitting diodes (μLED), and fluorescence emission is collected by an 8-by-64 single-photon avalanche diode (SPAD) array, together packaged to a width of 420 μm to allow deep insertion through a cannula. Each SPAD is masked by a repeating pattern of Talbot gratings that give each pixel a different angular sensitivity, allowing three-dimensional image reconstruction to a resolution of ~20 μm. The integrated imager is able to monitor fluorescent targets across a field of view of 1000 μm by 600 μm by 500 μm at arbitrary tissue depths.**

Keywords—**time-gated fluorescence imaging, single-photon avalanche diode, microLED, neural imaging**

I. Introduction

Deep-brain fluorescence imaging is challenged by the strong scattering and absorption of visible light in tissue. Scattering events, which occur as often as every 50 μm along a photon's trajectory in grey matter [1], cause photons to lose directionality quickly with depth in tissue. Multiphoton microscopy [2] or active resolution-enhancing methods such as super-resolution microscopy [3] are still limited to imaging depths of less than two millimeters in brain tissue.

One way to overcome these scattering and absorption limits is to implant waveguides to deliver light into and out of tissue. Graded index (GRIN) rod lenses (1.8 mm diameter) [4] and multimode fiber endoscopes (50 μm core diameter) [5] have successfully imaged neural structures several millimeters deep with microscope-level resolution. Nonetheless, their fields of view (FOVs) are inherently limited by the diameter of the waveguide, which can only be increased with a larger displaced insertion volume. This tradeoff between FOV and invasiveness makes waveguides an unsuitable solution for scanning large volumes in the deep brain.

Yet another approach to achieving depth is to insert an integrated imaging system into the brain itself, where photons are collected and converted into electrical signals locally without having to scatter or be transported through a waveguide. An integrated CMOS imager has been reported with micro-light-emitting diode (μLED) excited fluorescence emission collected with a CMOS photodetector array [6]. The difficulty here lies in miniaturizing optical components such as lenses, detectors, and interconnects for minimum invasiveness while maximizing resolution.

In this work, we address these challenges by fully integrating two μLED excitation sources and 512 single-photon-avalanche-
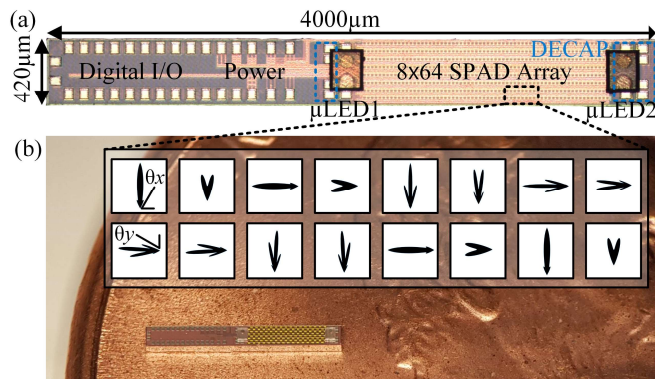

Fig. 1. (a) Die photo of the Deep-Brain Fluorescence Imager harboring 512 SPAD pixels and two μLEDs; decoupling capacitors are marked in blue. (b) Ideal amplitude responses of 16 unique Talbot gratings to angular modulation in *x, y* directions over a picture of the Imager on top of a penny.

diode (SPAD) photodetectors onto a CMOS integrated circuit (IC) measuring only 420 μm by 4 mm by 310 μm (Fig. 1a). Light generation on the chip avoids the losses and complexity of waveguide transmission. Imaging data are transmitted digitally on six wires at an effective data bandwidth of 37.5 MBps. With a width of only 420 μm, this chip can be attached to the end of a cannula of equal diameter. One of sixteen unique diffraction gratings in front of each SPAD in the array gives the pixels an angular sensitivity that allows for computational identification of source location, giving enhanced volumetric resolution at the depth of interest [7].

II. System Overview

Computationally reconstructing a fluorescent source in its FOV requires maximizing the signal-to-noise-and-background ratio (SNBR) achievable in each pixel. The noise is dominated by the shot noise in both observed counts and dark counts, and scattering in tissue. The background is dominated by excitation source photons that have not been successfully rejected.

Excitation background intensities are typically at least three orders of magnitude higher than the fluorescence signal, making this rejection challenging. In a typical fluorescence microscope, this is accomplished with a system of high-performance filters composed of absorptive and dichroic filters. In our case, it is not possible to integrate absorptive filters with sufficient rejection capabilities and maintain probe thicknesses of less than 50 μm [6]. Interference filters are much thinner, however, their rejection is highly dependent on incident angle, making them poor filters for oblique light. The pixels in this imager require

collection of light up to 60 degrees from normal incidence to allow for 3D reconstruction.

Because of these difficulties with spectral rejection of the excitation light, we choose to perform this rejection temporally by pulsing the excitation source and collecting the fluorescence signal after this excitation has been removed [8-10]. This relies on the fact that fluorescence emission lingers after the excitation with a characteristic exponential decay lifetime, which is typically on the scale of several nanoseconds for most fluorophores. Precise timing of digital clocks can turn a photodetector on immediately after the excitation source has been extinguished such that only fluorescence is collected. The excitation illumination is required to be have a sharp fall-time, shorter than the lifetime of the fluorophore. Detectors, in turn, are required to have sharp on-times and sufficient excitation rejection while in their off state. Precise clock synchronization must be achieved to maintain the relative timing between the turn off of the excitation source and the gating of the detector.

In large microscopy systems, the sharp turn-off of the light source is typically provided by an external laser. In this implanted system, we instead rely on pulsing two on-chip light-emitting diodes. Fig. 2 shows a circuit diagram of the imager fabricated in a 130-nm high-voltage CMOS process, including the two light emitters, SPAD detector array, and timing control. The clocking circuitry is implemented off chip on an FPGA.

Each on-chip µLED driver is a three-stage buffer chain with increasing fan-out resulting in a peak current drive of 70 mA at the final stage. Two commercial µLEDs (CREE TR2227, center wavelength 464 nm, 180 µm × 230 µm × 50 µm) are mounted on the surface of the chip with gold-stud bonding. Denoted as *µLED1* and *µLED2*, both µLEDs are driven by a common shutter signal *LEDON* delivered at 1.5-V logic levels. A level shifter shifts this low-voltage signal to a 5-V peak-to-peak drive signal, which is skewed to reduce the pull-down slew (to 700 ps with 100-pF loading, modeling the diffusion capacitance at an LED on-state) at the expense of the pull-up slew (2.2 ns). On-chip metal-insulator-metal capacitors between the anode (*LEDAN*) and cathode (*LEDCATH*), 35 and 75 pF on *µLED1* and *µLED2*, respectively, act as a charge reservoir for fast switching. An additional decoupling capacitance of 1 µF is implemented off chip between *LEDAN* and *LEDCATH*.

The 8-by-64 SPAD array, designed with a pixel pitch of 25.3 and 51.3 µm in the *x* and *y* directions, respectively, is driven by a global shutter *SPADON*, the turn-on edge of which is timed to occur a programmable length of time after the turn-off edge of *LEDON*. Each SPAD is designed with an active quenching and reset circuit (*RST* in Fig. 2) that toggles the SPAD into and out of Geiger mode with a 1.5-V change in the applied reverse bias around the breakdown voltage, which is measured to be 15.5 V. The SPAD is reverse biased with the global cathode (*SPADCATH*) held at a constant 17 V (1.5-V overvoltage), which has been chosen to optimize the trade-off between photon detection probability (12.4% for 530 nm) and dark count rate (40 Hz) [11]. Hot pixels, defined as pixels with counts larger than five times the median, take up 2% of the array and were silenced during further measurements. The SPADs can detect a single photon per 50-ns reset cycle, with a six-bit ripple counter accumulating photons to a dynamic range of 63. A finite state machine (FSM) implemented on the FPGA controls the data readout operation with a 100 MHz clock.
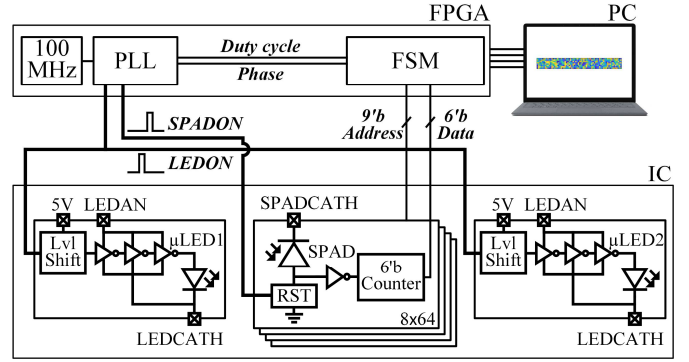

Fig. 2. System-level circuit diagram. Two µLEDs positioned on each side of the 8 by 64 SPAD array are pulsed with a sub-ns falling edge, and each SPAD pixel is designed to have a sharp a turn-on time using an active reset circuit (RST). An FPGA-implemented PLL produces two clocks with programmable duty cycle and phase to control the relative time delay between global-shutter signals *SPADON* and *LEDON*.

A phase-locked loop (PLL), locked to a 100 MHz internal clock, produces both clock signals *LEDON* and *SPADON* with controllable duty cycles and phase shifts. A 900-MHz clock internal to the FPGA, further divided into eight phases, allows the rising and falling edges of both signals to be positioned with a resolution of 140 ps. At this resolution, determination of the fluorescence lifetime of the fluorophore is also possible [8].

The frame rate can reach a maximum of 50 kfps at high signal conditions, limited by the settling time constraint of the FPGA I/O interface multiplied by the number of pixels. It is more practically limited, however, by the maximum irradiance of the µLEDs which is not capable of saturating pixels at a forward bias of 5 V, requiring longer integration windows.

The IC consumes 6 mW without the µLED under pixel-saturating conditions, and the µLEDs together consume an average power of 20-40 mW when pulsed at 6% duty cycle with forward bias voltages of 4-5 V, respectively. 32 voltage and signal wires are supplied externally through a bundle of wires along the length of the cannula, with careful grounding to prevent coupling between time-critical transmission lines. We can expect the number of wires to be reduced with voltage regulators and timing control circuitry implemented on-chip.

III. FLUORESCENCE IMAGING

A. Time-Gated Fluorescence Imaging

An instrument response function (IRF) of the SPAD detectors themselves is first characterized with a 50-ps pulse width laser (Fianium SC450-PP) incident normally to the SPAD with 80 µW average power (Fig. 3b, *Laser*). The laser's fast pulse can be approximated as an ideal delta function; as a result, the measured response is the IRF of the SPAD device.

Fig. 3a shows the imager with the µLEDs pulsed at a repetition rate of 20 MHz and 6% duty cycle, at a forward bias voltage of 4.2 V. The fast pulsing of the µLEDs is measured by a SPAD pixel in Fig. 3b. A 7% duty-cycled *SPADON* window, shrunk into an effective 2% window due to internal circuit delays, is shifted relative to the *LEDON* signal by steps of 140 ps, yielding a photon count which is the convolution of the µLED pulse and the IRF of the SPAD detector. Normalized photon counts are plotted for anode voltages ranging from 4 to 5 V with the cathode set at 0 V.
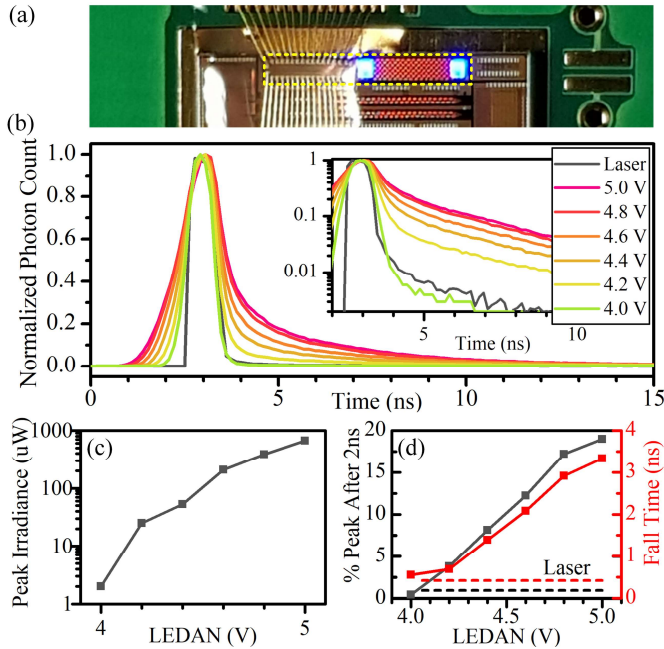
Fig. 3. (a) Imager with μLEDs illuminated at 40 mA on-state current. (b) Pulsed μLED illumination measured with the time-gated SPAD array and normalized at different μLED forward bias voltages; inset in log scale. A 50-ps laser pulse is measured in comparison. (c) Peak on-state irradiance, (d) percentage of excitation irradiance 2 ns after the peak intensity (left axis), and 90-10 percentile fall time of the μLEDs plotted versus anode voltage (right axis). Dotted lines show %-of-peak and fall time measured for Fianium laser.
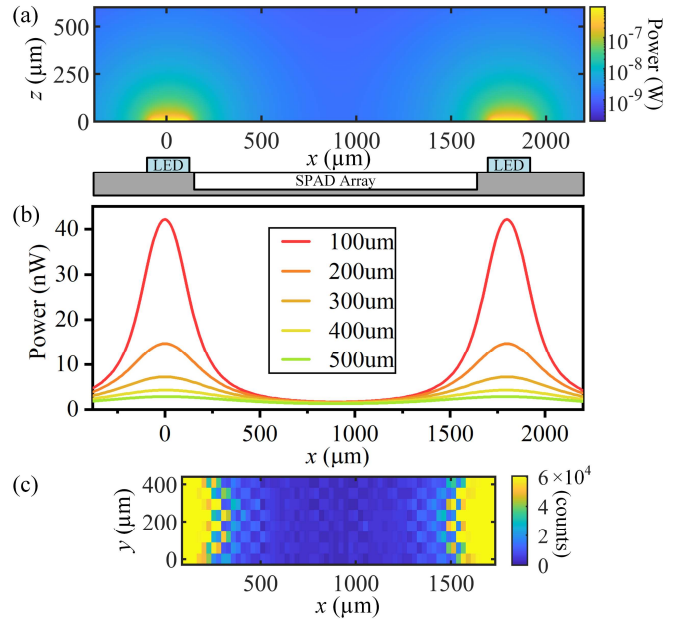
Fig. 4. (a) μLED intensity experienced by a 10 μm-diameter soma at different coordinates above the imager, in log scale, where z is the distance away from the imager. (b) Line scans of (a) at different z distances; a peak radiation of 50 μW was assumed for each LED. (c) Raw counts of 512-pixel array acquired with μLEDs illuminated in absence of imaging target, acquired for 0.125 s.

Fig. 3c shows that a higher forward bias on the μLED increases the forward current, producing more irradiance as measured by a power meter (Thorlabs PM100D). However, higher μLED output power results in slower turn off times, as shown in Fig. 3d. With time gating for background rejection, this results in a tradeoff between fluorescence signal intensity, which is directly proportional to peak μLED irradiance, and signal background, which is dominated by the amount of μLED irradiance remnant after the SPAD detector is gated on. Assuming a time delay of 2 ns between the peak irradiance and the onset of the SPAD time gate, the percentage of the peak excitation irradiance remaining after the μLED is turned off is plotted in Fig. 3d for different μLED forward bias voltages. The fall times (90-percent-to-10-percent) of the μLED irradiance are also plotted, confirming that the temporal characteristics of the μLED become slower with higher bias voltage. Measurements for the ps laser pulse, drawn as dashed lines in Fig. 3d, show a 1% trailing illumination intensity after its peak with the same gating delay of 2 ns, and a 417-ps fall time. The μLED matches the fast temporal characteristics of the laser at forward bias voltages below 4.2 V, which are at peak irradiance levels below 25 uW. At low irradiance, the imager will be required to accumulate for longer periods of time and may reduce the effective frame rate. Higher forward bias voltages may be used in cases of high signal intensity, e.g. imaging large fluorescent clusters, to reduce frame rate at the cost of a reduced signal-to-background ratio (SBR).

B. Radiation Profile

The μLEDs are designed to face the same direction as the SPAD array in order to minimize the amount of direct irradiance traveling into the SPADs, which worsens the IRF and lowers SBR in the case of incomplete excitation rejection. As shown in Fig. 1a, the μLEDs are located on either side of the imaging array. Since some areas of the FOV are located closer to the μLEDs than others, illumination intensities are nonuniform, producing an unevenly weighted fluorescence image. Fig. 4a shows a simulated side view of the radiation power produced by the two μLEDs, located at $x = 0$ and 1800 μm, perceived by a 10-μm-diameter circular collection volume modeling a single soma. The side view of the imager is illustrated, in scale, in Fig. 4a.

Fig. 4b plots the cross section of the radiation power in Fig. 4a at different coordinates in the FOV, when illuminated with a peak irradiance of 50 μW from each μLED. Individual curves show line-scans of the received irradiance at five different distances from the surface of imager. The measured irradiance directly above the μLED varies from 42 nW at 100 μm distance to 2.9 nW at 500 μm. This uneven illumination means that different locations of the tissue volume will experience different irradiances and the fluorescence collected by the SPADs will similarly reflect this nonuniformity.

Background rejection is also made more difficult by this nonuniformity. Fig. 4c shows a measurement of the raw SPAD counts created by the direct irradiance of μLED, accumulating for 125 ms with μLEDs at a 4-V forward bias. Pixels on the left and right ends of the array show saturated counts because of their proximity to the μLEDs. In the case of incomplete rejection of excitation photons, these pixels are likely to to have much higher background levels.

In the center of the SPAD array ($x = 900$ μm) where the radiation profile becomes relatively uniform, however, the received irradiance only varies from 1.69 to 1.30 nW for z distances 100 through 500 μm (Fig. 4b). In fact, the irradiance across a tissue volume of 1000 μm (x) × 600 μm (y) ×

500 μm (z) centered above the photodetector array varies less than a factor of two, allowing for wide-view single-shot imaging in this region. This defines the effective FOV of the imager.

C. Image Reconstruction using Talbot Gratings

The sixteen different Talbot grating structures, implemented on M1, M3, and M5 layers of the CMOS metal stack, create a unique incident-angle-sensitivity for the SPAD pixels [10, 12]. The imager uses this diversity to convert a two-dimensional SPAD count into a three-dimensional backprojected image [7]. For this, a mapping matrix A must be constructed to satisfy $y = Ax$, where y is the 512-pixel SPAD count, x is the n-voxel image, and A is a matrix that describes how many photon counts every voxel induces in every SPAD pixel. We define our imaging volume to be the $1000 \times 600 \times 500\ \mu m^3$ volume centered above the SPAD array with a 10 μm voxel grid size, resulting in a 512-by-360,000 A matrix. It is constructed from measurements of the angular modulation of the sixteen different Talbot grating structures [10], as well as our knowledge of the relative location of each pixel and voxel. Given a SPAD array measurement y, the backprojection $x = A^+y$ yields the least-mean-squares error solution of the 3D image, where A^+ is the pseudoinverse matrix of A.

D. Fluorescent Phantom Imaging

To construct a phantom imaging target, fluorescent microspheres of 10-μm diameter (Polysciences, Fluoresbrite YG) were deposited on a sheet of cover glass with cluster sizes ranging from 40 to 400 μm in diameter (Fig. 5a-d). The cover glass was placed on top of the imager with a 400-μm spacer. μLEDs were pulsed at 10% duty cycle with a 20-MHz repetition rate while being forward biased at 4 V, producing a peak irradiance of 90 μW from each μLED. The SPADs were gated a 2-ns delay after the irradiance peak, for a total photon accumulation time of 125 ms.

Fig. 5e-h show SPAD counts in the imaging volume subtracted by counts acquired from an empty cover glass. The 400-μm distance between the SPAD array and source creates an intensity blur around the center of the cluster, owing to the 60-degree viewing angle of each pixel, while the checkerboard-like intensity map shows the alternating angular modulation directions in x and y. The cluster in Fig. 5d, in contrast with Fig. 5c, is too small in fluorescence intensity to produce identifiable counts associated with its location.

Fig. 5i shows the backprojection of the bead cluster in Fig. 5c at four z heights ranging from 100 to 400 μm. The ideal point spread function of the SPAD array (Fig. 5j) offers a comparison with the z-slice at 400 μm, showing a full width at half maximum resolution of ~20 μm in x, y, and z directions.

IV. Conclusion

In this paper, we present a fully integrated implantable three-dimensional fluorescence imager. Fluorescence excitation is provided by two fast-pulsed μLEDs, and fluorescence emission is collected by a 512-pixel SPAD array. Time-gated fluorescence imaging is implemented to reject excitation light without the need for optical filters. The system fits within the width of a 420-μm cannula for deep brain insertion.

In this time-gated approach, a tradeoff exists between peak μLED irradiance and excitation rejection. SBR is highest at low
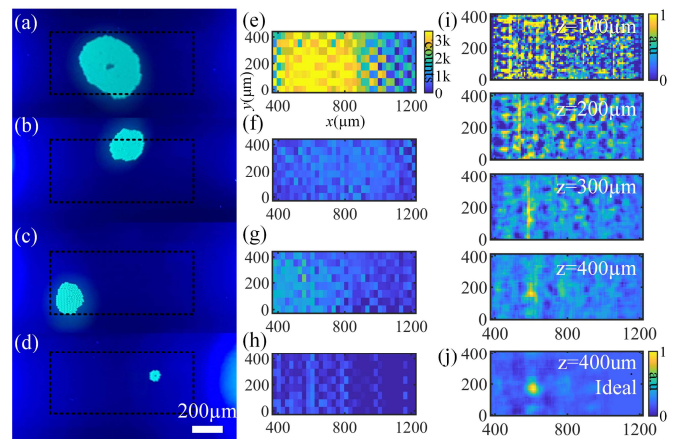

Fig. 5. (a-d) Microscope images of various fluorescent bead clusters deposited on a cover glass 400 μm above the imager; imager FOV is marked in black dashes. (e-h) Corresponding SPAD counts of the imager corrected for nonuniform illumination. (i) z-slices of backprojection of Fig. 5c scene and (j) simulation of an ideal point spread function.

irradiance conditions; however, image acquisition under such conditions forces a low frame rate and still remains more than an order of magnitude lower than commercial spectral filters. Excitation rejection could be improved with faster μLED turnoff. We compensate for the nonuniform illumination profile produced by the μLEDs by relying on the relative uniformity of illumination in the volume centered above the SPAD array.

References

[1] S. L. Jacques, "Optical properties of biological tissues: a review," *Phys Med Biol,* vol. 58, no. 11, pp. R37-61, Jun 7 2013.

[2] T. Wang *et al.*, "Three-photon imaging of mouse brain structure and function through the intact skull," *Nat Methods,* vol. 15, no. 10, pp. 789-792, Oct 2018.

[3] A. Dani, B. Huang, J. Bergan, C. Dulac, and X. Zhuang, "Superresolution imaging of chemical synapses in the brain," *Neuron,* vol. 68, no. 5, pp. 843-56, Dec 9 2010.

[4] O. Skocek *et al.*, "Author Correction: High-speed volumetric imaging of neuronal activity in freely moving rodents," *Nat Methods,* vol. 15, no. 6, p. 469, Jun 2018.

[5] S. A. Vasquez-Lopez *et al.*, "Subcellular spatial resolution achieved for deep-brain imaging in vivo using a minimally invasive multimode fiber," *Light Sci Appl,* vol. 7, p. 110, Dec 19 2018.

[6] Y. Sunaga *et al.*, "Implantable imaging device for brain functional imaging system using flavoprotein fluorescence," *Jpn J Appl Phys,* vol. 55, no. 3, Mar 2016.

[7] A. Wang, P. Gill, and A. Molnar, "Light field image sensors based on the Talbot effect," *Appl Opt,* vol. 48, no. 31, pp. 5897-905, Nov 1 2009.

[8] D. E. Schwartz, E. Charbon, and K. L. Shepard, "A Single-Photon Avalanche Diode Array for Fluorescence Lifetime Imaging Microscopy," *IEEE J Solid-State Circuits,* vol. 43, no. 11, pp. 2546-2557, Nov 21 2008.

[9] D. Mosconi, D. Stoppa, L. Pancheri, L. Gonzo, and A. Simoni, "CMOS single-photon avalanche diode array for time-resolved fluorescence detection," *Proc Eur Solid-State,* pp. 564-+, 2006.

[10] C. Lee *et al.*, "11.5 A 512-Pixel 3kHz-Frame-Rate Dual-Shank Lensless Filterless Single-Photon-Avalanche-Diode CMOS Neural Imaging Probe," in *2019 IEEE International Solid-State Circuits Conference-(ISSCC),* 2019: IEEE, pp. 198-200.

[11] R. M. Field, J. Lary, J. Cohn, L. Paninski, and K. L. Shepard, "A low-noise, single-photon avalanche diode in standard 0.13 μm complementary metal-oxide-semiconductor process," *Applied Physics Letters,* vol. 97, no. 21, 2010.

[12] C. Lee, B. Johnson, T. Jung, and A. Molnar, "A 72 x 60 Angle-Sensitive SPAD Imaging Array for Lens-less FLIM," *Sensors (Basel),* vol. 16, no. 9, Sep 2 2016.